TESS Shines Light on the Origin of the Ambiguous Nuclear Transient ASASSN-18el

Jason T. Hinkle,[1] Christopher S. Kochanek,[2,3] Benjamin J. Shappee,[1] Patrick J. Vallely,[2] Katie Auchettl,[4,5,6]
Michael Fausnaugh,[7] Thomas W.-S. Holoien,[8,*] Helena P. Treiber,[1,9] Anna V. Payne,[1,†] B. Scott Gaudi,[2]
Jose L. Prieto,[10,11] Keivan G. Stassun,[12] Todd A. Thompson,[2,3] John L. Tonry,[1] and Steven Villanueva Jr.[13,‡]

[1]Institute for Astronomy, University of Hawai'i, 2680 Woodlawn Drive, Honolulu, HI 96822, USA
[2]Department of Astronomy, The Ohio State University, 140 West 18th Avenue, Columbus, OH 43210, USA
[3]Center for Cosmology and Astroparticle Physics, The Ohio State University, 191 W. Woodruff Avenue, Columbus, OH 43210, USA
[4]School of Physics, The University of Melbourne, Parkville, VIC 3010, Australia
[5]ARC Centre of Excellence for All Sky Astrophysics in 3 Dimensions (ASTRO 3D)
[6]Department of Astronomy and Astrophysics, University of California, Santa Cruz, CA 95064, USA
[7]Department of Physics and Kavli Institute for Astrophysics and Space Research, Massachusetts Institute of Technology, Cambridge, MA 02139, USA
[8]The Observatories of the Carnegie Institution for Science, 813 Santa Barbara Street, Pasadena, CA 91101, USA
[9]Department of Physics and Astronomy, Amherst College, C025 New Science Center, 25 East Dr., Amherst, MA 01002-5000, USA
[10]Núcleo de Astronomía de la Facultad de Ingeniería y Ciencias, Universidad Diego Portales, Av. Ejército 441, Santiago, Chile
[11]Millennium Institute of Astrophysics, Santiago, Chile
[12]Department of Physics and Astronomy, Vanderbilt University, Nashville, TN 37235, USA
[13]NASA Goddard Space Flight Center, Exoplanets and Stellar Astrophysics Laboratory (Code 667), Greenbelt, MD 20771, USA

ABSTRACT

We analyze high-cadence data from the Transiting Exoplanet Survey Satellite (TESS) of the ambiguous nuclear transient (ANT) ASASSN-18el. The optical changing-look phenomenon in ASASSN-18el has been argued to be due to either a drastic change in the accretion rate of the existing active galactic nucleus (AGN) or the result of a tidal disruption event (TDE). Throughout the TESS observations, short-timescale stochastic variability is seen, consistent with an AGN. We are able to fit the TESS light curve with a damped-random-walk (DRW) model and recover a rest-frame variability amplitude of $\hat{\sigma} = 0.93 \pm 0.02$ mJy and a rest-frame timescale of $\tau_{DRW} = 20^{+15}_{-6}$ days. We find that the estimated τ_{DRW} for ASASSN-18el is broadly consistent with an apparent relationship between the DRW timescale and central supermassive black hole mass. The large-amplitude stochastic variability of ASASSN-18el, particularly during late stages of the flare, suggests that the origin of this ANT is likely due to extreme AGN activity rather than a TDE.

Keywords: Accretion(14) — Active galactic nuclei(16) — Black hole physics (159) — Supermassive black holes (1663) — Tidal disruption (1696)

1. INTRODUCTION

Active galactic nuclei (AGNs) are the actively accreting supermassive black holes (SMBHs) found at the centers of $\sim 1 - 5\%$ of galaxies in the local universe (e.g., Ho 2008; Haggard et al. 2010; Lacerda et al. 2020). For decades, it has been known that AGNs vary stochas-tically both photometrically (e.g., Ulrich et al. 1997; Drake et al. 2009; MacLeod et al. 2012) and spectro-scopically (e.g., Bianchi et al. 2005). Due to the recent growth of optical transient surveys, AGNs and quiescent galaxies alike have also been found to undergo extreme flaring behavior. Such events include tidal disruption events (TDEs; van Velzen et al. 2011; Gezari et al. 2012; Holoien et al. 2014a, 2016a; Payne et al. 2021; Hinkle et al. 2021b), dramatic changes in the accretion rates of known AGNs (e.g., Denney et al. 2014; Shappee et al. 2014; Wyrzykowski et al. 2017; Trakhtenbrot et al. 2019a; Frederick et al. 2019, 2021), and a growing class

Corresponding author: Jason T. Hinkle
jhinkle6@hawaii.edu

* NHFP Einstein Fellow
† NASA Fellowship Activity Fellow
‡ NPP Fellow

of ambiguous nuclear transients (ANTs; Neustadt et al. 2020; Hinkle et al. 2021c; Holoien et al. 2021).

Broadly, nuclear transients share a set of observed characteristics including bright ultraviolet (UV) emission (e.g., Holoien et al. 2016a; Neustadt et al. 2020; Hinkle et al. 2021c), strong emission lines (Holoien et al. 2014a; Trakhtenbrot et al. 2019a; Leloudas et al. 2019), slow and often smooth photometric evolution (Frederick et al. 2021; Hinkle et al. 2020; van Velzen et al. 2021), and, for some events, X-ray emission (Holoien et al. 2016a; Neustadt et al. 2020; Hinkle et al. 2021b). These different classes of nuclear transients often have distinct properties in their X-ray continua, color evolution, and prescence of light curve rebrightening episodes (e.g., Frederick et al. 2021). However, in the case of ANTs, the lack of expected features or the presence of unexpected features can make a definitive classification difficult (Neustadt et al. 2020; Frederick et al. 2021; Hinkle et al. 2021c; Malyali et al. 2021; Holoien et al. 2021).

One example of an ANT is ASASSN-18el (AT2018zf[1]; Nicholls et al. 2018; Trakhtenbrot et al. 2019b). ASASSN-18el was discovered by the All-Sky Automated Survey for Supernovae (ASAS-SN; Shappee et al. 2014; Kochanek et al. 2017) on 2018 March 3 in a known AGN, 1ES 1927+654 (Giacconi et al. 1979). Archival spectra were that of a "true" Type 2 AGN, with narrow lines and no broad lines even in polarized light (Boller et al. 2003; Tran et al. 2011). Pre-discovery imaging from the Asteroid Terrestrial-impact Last Alert System (ATLAS; Tonry et al. 2018a) indicates that the source became active as early as 2017 December 23 (Trakhtenbrot et al. 2019b).

Spectroscopic follow-up of the flare found that the AGN had broad emission lines, suggesting that ASASSN-18el was an optical changing-look AGN (CL-AGN, e.g., Shappee et al. 2014; Denney et al. 2014; LaMassa et al. 2015), changing from a Seyfert 2 to a Seyfert 1 over the course of several months. During the optical flare, the X-ray flux dropped by several orders of magnitude (Trakhtenbrot et al. 2019b; Ricci et al. 2021; Laha et al. 2022) and the dominant X-ray component softened from a hard power-law typical of an AGN (e.g., Ricci et al. 2017) to a more TDE-like blackbody spectrum (e.g., Auchettl et al. 2017). Based on the X-ray evolution and smooth UV/optical flare, Ricci et al. (2020) speculated that ASASSN-18el was a TDE. Nonetheless, the overall properties of ASASSN-18el make a definitive distinction between an AGN flare and TDE difficult.

---

[1] https://www.wis-tns.org/object/2018zf

In this paper, we analyze photometry of ASASSN-18el from the Transiting Exoplanet Survey Satellite (TESS; Ricker et al. 2015), additional late-time optical light curves, and late-time X-ray light curves from the Neutron Star Interior and Composition Explorer (NICER; Gendreau et al. 2012) to understand the emission of ASASSN-18el in the growing context of nuclear flares. This paper is organized as follows. In Section 2 we detail the data used in this work. In Section 3 we present our analysis and then discuss our results in Section 4. Finally, we summarize our findings in Section 5. Throughout the paper, we assume a cosmology of $H_0 = 69.6$ km s^{-1} Mpc^{-1}, $\Omega_M = 0.29$, and $\Omega_\Lambda = 0.71$ (Wright 2006; Bennett et al. 2014). The source redshift of z = 0.01905 implies a luminosity distance of 83.3 Mpc and the Galactic foreground extinction in the direction of ASASSN-18el is $A_V = 0.236$ mag (Schlafly & Finkbeiner 2011). Trakhtenbrot et al. (2019b) measured a virial mass of $M_{BH} = 1.9 \times 10^7 M_\odot$ using spectra from their follow-up campaign, which we adopt in this manuscript. As this is a single epoch measurement, we will assume an uncertainty of 0.3 dex (e.g., Guo et al. 2020).

2. DATA

Data near peak emission and up to roughly 400 days after were presented originally in Trakhtenbrot et al. (2019b), with additional X-ray data shown in Ricci et al. (2021) and X-ray/UV data shown in Laha et al. (2022). Here we re-reduce ground-based survey data on ASASSN-18el from ASAS-SN and ATLAS, now extending roughly 1300 days after peak. We additionally use TESS, Swift, NICER, and ground-based follow-up data. In this section we describe the procedures used to obtain and reduce these data.

2.1. *ASAS-SN Data*

The ASAS-SN transient survey consists of five sites located at Haleakalā Observatory, McDonald Observatory, the South African Astrophysical Observatory (SAAO), and two at Cerro Tololo Inter-American Observatory (CTIO), all hosted by the Las Cumbres Observatory (Brown et al. 2013). Each site hosts four telescopes on a common mount, and the telescopes are 14-cm aperture Nikon telephoto lenses with 8″0 pixels. However, at the time of the discovery of ASASSN-18el, ASAS-SN operated with two units taking V-band images and three units taking g-band images. After the seasonal break following the transient peak emission, ASAS-SN had fully switched to g-band imaging and all of the later time ASAS-SN data are in the g-band.

The images were reduced using the automated ASAS-SN pipeline (Shappee et al. 2014), which uses the ISIS
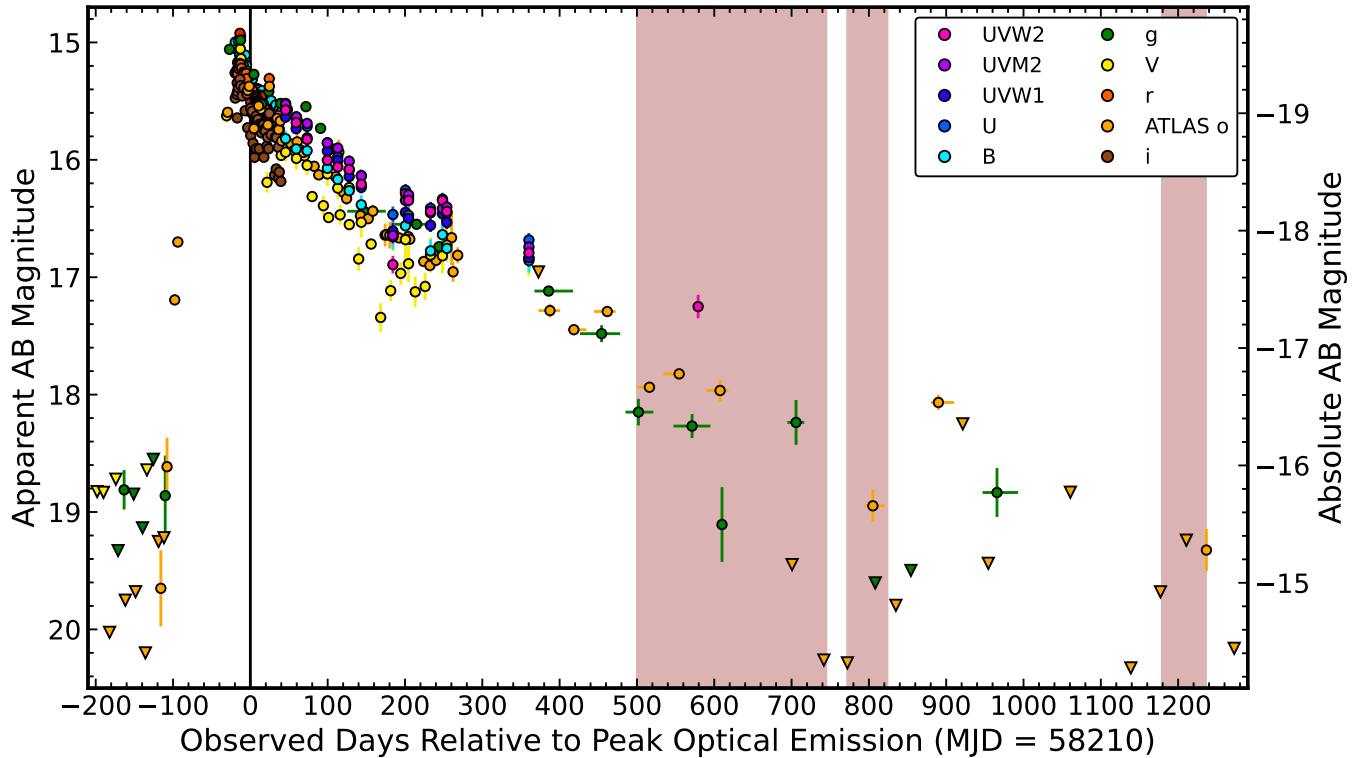
Figure 1. Optical and UV light curves of ASASSN-18el, showing ASAS-SN (gV), ATLAS (o), Swift ($UBV + UV$), and other ground-based ($BVrRiI$) photometry. The photometry shown here spans from roughly 200 days prior to peak optical emission in the ATLAS o-band to roughly 1250 days after in observer-frame days. The vertical red bands indicate time periods with TESS coverage. The vertical black line indicates the time of the ATLAS o-band peak. Horizontal error bars indicate the date range of observations stacked to obtain deeper limits and higher S/N detections, although for some data they are smaller than the symbols. Downward-facing triangles indicate 3σ upper limits. All data are corrected for Galactic extinction and are shown in the AB system.

image subtraction package (Alard & Lupton 1998; Alard 2000). We then used the IRAF `apphot` package with a 2-pixel radius (approximately $16''.0$) aperture to perform aperture photometry on each subtracted image, to produce a differential light curve. We calibrated our photometry using the AAVSO Photometric All-Sky Survey (Henden et al. 2015). To obtain good detections or limits throughout the transient evolution, we stacked the ASAS-SN epochs. We used 10-day bins prior to and during the flare for both V- and g-band data, and 50-day bins for the g-band data after the seasonal break to sample the decline. We excluded ASAS-SN data more than 1000 days after peak optical emission as contamination from the residuals of a nearby star became similar in amplitude to the transient.

2.2. ATLAS Data

At the time of discovery, ATLAS consisted of two 0.5-m f/2 Wright Schmidt telescopes located on Haleakalā and at the Mauna Loa Observatory. The ATLAS telescopes typically obtain four 30-second exposures of 200–250 fields per night, covering roughly a quarter of the sky visible from Hawai'i each night (Smith et al. 2020). Depending on the Moon phase, ATLAS uses either the 'cyan' (c) filter from 420–650 nm or the 'orange' (o) filter covering the 560–820 nm range (Tonry et al. 2018a). As there was little c-band coverage of the flare, particularly in the late phases where we focus our study, we have excluded it from our analysis.

The ATLAS images are processed by a pipeline that includes flat-field, astrometric, and photometric calibrations. We performed forced photometry on the subtracted ATLAS images of ASASSN-18el as described in Tonry et al. (2018a) to create a differential light curve. Due to the bright host galaxy and nearby stars there are many epochs with artifacts remaining in the subtracted images, as indicated by the high reduced χ^2 of the PSF fits. We therefore excluded images with reduced $\chi^2 > 10$. Similar to our ASAS-SN light curves, we combined individual epochs to increase the S/N. Prior to the flare, we combined the data in 10-day bins, during the flare we combined the four intra-night observations, and after the seasonal break we stacked in 30-day bins.

2.3. *Additional Photometry*

We also obtained $BVrRiI$ data from several ground-based observatories. These include the Las Cumbres Observatory Global Telescope (LCOGT) network (Brown et al. 2013), the 0.5-m DEdicated MONitor of EXotransits and Transients (DEMONEXT; Villanueva et al. 2016, 2018), the 0.5-m Iowa Robotic Telescope, and the Post Observatory.

We reduced these data using typical procedures including flat-field corrections and then obtained the astrometry for each image using astrometry.net (Barron et al. 2008; Lang et al. 2010). For these ground-based data we used `apphot` to measure $5''.0$ aperture magnitudes of the host plus transient emission, and subtracted the $5''.0$ host flux computed by Hinkle et al. (2021a). We used REFCAT (Tonry et al. 2018b) magnitudes of stars in the field and the corrections of Lupton (2005) for calibration. We stacked all of this ground-based photometry in 1 day bins as the source was bright and there were several facilities taking images concurrently.

We also use the Swift $UBV + UV$ photometry of ASASSN-18el presented in Hinkle et al. (2021a). Some of these data were originally presented in Trakhtenbrot et al. (2019b), but were re-reduced in Hinkle et al. (2021a) to account for corrected calibration files for the Swift UV filters. Figure 1 shows the light curves of ASASSN-18el from ASAS-SN, ATLAS, Swift and ground-based observatories in AB magnitudes and corrected for Galactic foreground extinction.

2.4. *TESS Observations*

The host galaxy of ASASSN-18el lies close to the North Ecliptic Pole and the TESS northern continuous viewing zone. It was observed in each sector of Cycle 2 except for Sector 24. The source was very close to the edge of the chip in Sector 14, and therefore we do not include this sector. This allowed us to get a high-cadence and high-precision light curve beginning roughly 500 days after the peak optical emission. The source was also observed again in Sectors 40 and 41 of Cycle 4.

The differential light curves are generated from the TESS full frame images (FFIs) following the procedures of Vallely et al. (2019, 2021). Because the TESS PSF has non-trivial structure and the camera orientations rotate between sectors, we constructed independent reference images for each sector. We selected the first 100 FFIs of good quality obtained in each sector, excluding images with above average sky background levels or PSF widths. We also excluded FFIs that were affected by an instrument anomaly, showed significant backgrounds due to scattered light, had data quality flags, or a com-

promised spacecraft pointing. We converted the measured fluxes into TESS-band magnitudes using an instrumental zero point of 20.44 electrons per second in the FFIs (TESS Instrument Handbook; Vanderspek et al. 2018).

2.5. *NICER Observations*

Throughout the evolution of ASASSN-18el, X-ray observations were obtained using NICER (Gendreau et al. 2012), an external payload on the International Space Station. NICER observed ASASSN-18el a total of 431 times between 2018 May 22.8 and 2021 February 17.7 (ObsIDs: 1200190101−1200190287, 2200190201−2200190370, and 3200190301−3200190451; PI: Kara).

The NICER data were reduced using NICERDAS version 6a and HEASOFT version 6.26.1. We applied standard filtering criteria in NICERL2. These criteria include[2]: a *NICER* pointing of ANG_DIST <0.015 degrees from the source location and exclusion of events during a South Atlantic Anomaly passage or when Earth was $30°$ $(40°)$ above the dark (bright) limb. We also removed events which were flagged as overshoot or undershoot events (EVENT_FLAGS=bxxxx00), and used the "trumpet filter" to remove events with a PI_RATIO $> 1.1+120/\text{PI}$ (Bogdanov et al. 2019).

To extract count rates for each epoch, we used XS-ELECT, and the standard ancillary response (ARF; nixtiaveonaxis20180601v002.arf) and response matrix (RMF; nixtiref20170601v001.rmf) files from the *NICER* CALDB. We assumed a photon index of 1.7 and the Galactic column density of 6.4×10^{20} cm^{-2} (Ricci et al. 2020) to convert the count rates to fluxes. Data within $\sim$500 days of peak optical emission were presented in Ricci et al. (2021). Here we extend the NICER data coverage until nearly 1100 days after peak to trace the X-ray luminosity evolution at late times.

3. ANALYSIS

3.1. *Optical Light Curve*

In addition to the pre-flare and near-peak data presented in Trakhtenbrot et al. (2019b), the light curves shown in Figure 1 now extend several years after the peak emission of the transient. It is clear that at the beginning of the TESS observations of ASASSN-18el, the transient is still detectable in both the stacked ASAS-SN g-band and the ATLAS o-band data.

---

[2] See   https://heasarc.gsfc.nasa.gov/docs/nicer/data_analysis/nicer_analysis_guide.html or (Bogdanov et al. 2019) for more details.
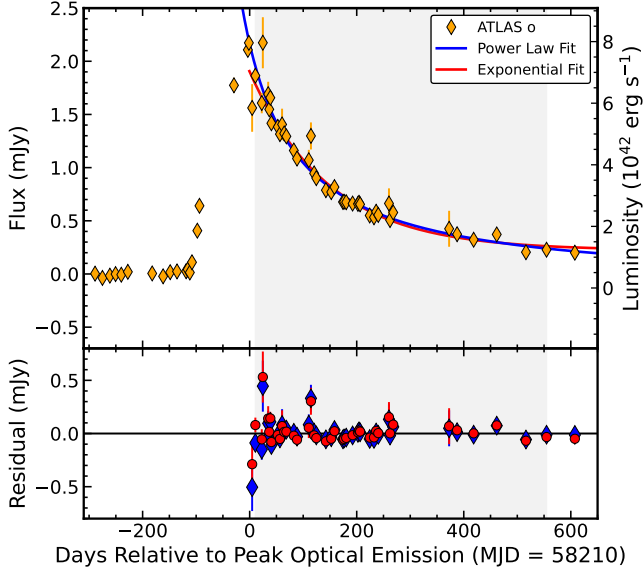
Figure 2. *Top panel*: ATLAS *o*-band light curve (orange diamonds) and the best-fitting power-law (exponential-decay) model in blue (red). The light gray shaded region shows the time period included in the fits. *Bottom panel*: The residuals of the models, shown in the same color as the fits themselves.

To obtain a time of peak optical light, we fit a parabola to the ATLAS *o*-band light curve as it is the most complete on both sides of the peak. Since the cadence is low, we fit the parabola over a wide date range of dates between MJD = 58116.2 and MJD = 58292.5. We generated 10,000 realizations of the ATLAS light curve over this date range with each flux perturbed by its uncertainty assuming Gaussian errors. We then fit a parabola to each of the perturbed light curves and took the median value as the peak of the distribution and used the 16th and 84th percentiles as the uncertainties. This leads to a time of peak *o*-band emission of MJD = 58210 ± 2 with a peak flux of 1.9 ± 0.1 mJy. Several studies of TDE flares have found significant offsets between the peak times in different optical bands (Holoien et al. 2019, 2020; Hinkle et al. 2021b) although the cadence of ASAS-SN data and the lack of UV data near peak preclude such comparisons.

One distinguishing feature of TDE light curves is that they are commonly described by a power-law decline in flux. In particular, when the mass per unit binding energy is constant, the decline slope is $t^{-5/3}$ (e.g., Evans & Kochanek 1989). To examine the decline slope of ASASSN-18el in the context of TDEs, we fit the ATLAS *o*-band flux as

$$f = f_{10} \left(\frac{t - t_0}{10 \text{ days}} \right)^{\alpha} + h \qquad (1)$$

to estimate the time t_0, the flux 10 days later f_{10}, the flux offset h, and the power-law index α. We fit the ATLAS data from 10 days after peak to MJD = 58817.5. An MCMC fit yields best-fit parameters of $t_0(\text{MJD}) = 58101^{+17}_{-14}$, $f_{10} = 28^{+12}_{-10}$ mJy, $h = -0.10^{+0.06}_{-0.09}$ mJy, and $\alpha = -1.05^{+0.15}_{-0.12}$ and this model is shown in Figure 2. This decline is consistent with the UV decline slope of $\alpha = -0.91 \pm 0.04$ measured by Laha et al. (2022). This decline slope is significantly flatter than expected for TDEs (e.g., Rees 1988; Phinney 1989), consistent with the qualitative comparison shown in Trakhtenbrot et al. (2019b).

The root mean squared (RMS) residuals from the power-law fit are 0.11 mJy after subtracting the median ATLAS flux uncertainty (e.g., Vaughan et al. 2003). For the remaining calculations of the RMS scatter, we subtract the median flux uncertainty to correct for the contribution of statistical noise to the observed variability.

We next fit the decline of ASASSN-18el using an exponential-decay model

$$f = ae^{-(t-t_{peak})/\tau_{decay}} + c \qquad (2)$$

similar to what has been done for some TDEs (e.g., Holoien et al. 2014b, 2016a,b; Payne et al. 2021). Here we set t_{peak} of MJD = 58210 from our fit to the ATLAS *o*-band light curve and fit the ATLAS data over the same time period to find best-fit parameters of $a = 1.69^{+0.07}_{-0.06}$ mJy, $\tau_{decay} = 147^{+11}_{-10}$ days, and $c = 0.22 \pm 0.02$ mJy. This model is shown in Figure 2 and it also provides a reasonable description of the data, with RMS residuals of 0.15 mJy. The best-fit $\tau_{decay} \sim 147$ days is roughly three times longer than found for typical TDEs (Holoien et al. 2014b, 2016a,b).

We next compare the RMS measurements obtained from the decline fits to the RMS scatter in the archival ATLAS light curve. Only considering data taken before the beginning of the rise on MJD $\simeq 58110$, we find an RMS scatter of 0.02 mJy in the ATLAS o-band data, suggesting that the transient is significantly more variable than the host galaxy was in quiescence.

3.2. *TESS Light Curve*

With our TESS light curve, we are able to study the variability properties of ASASSN-18el in great detail. In order to understand this variability in the context of AGN, we used a damped random walk (DRW) model (e.g., Kelly et al. 2009; Kozłowski et al. 2010; MacLeod et al. 2010; Zu et al. 2011; MacLeod et al. 2012; Zu et al. 2013) to fit the variability seen in Figure 3. Fundamentally, a DRW variability model assumes that the power spectral density (PSD) of an AGN can be described by a flat spectrum (white noise) at low frequencies, with
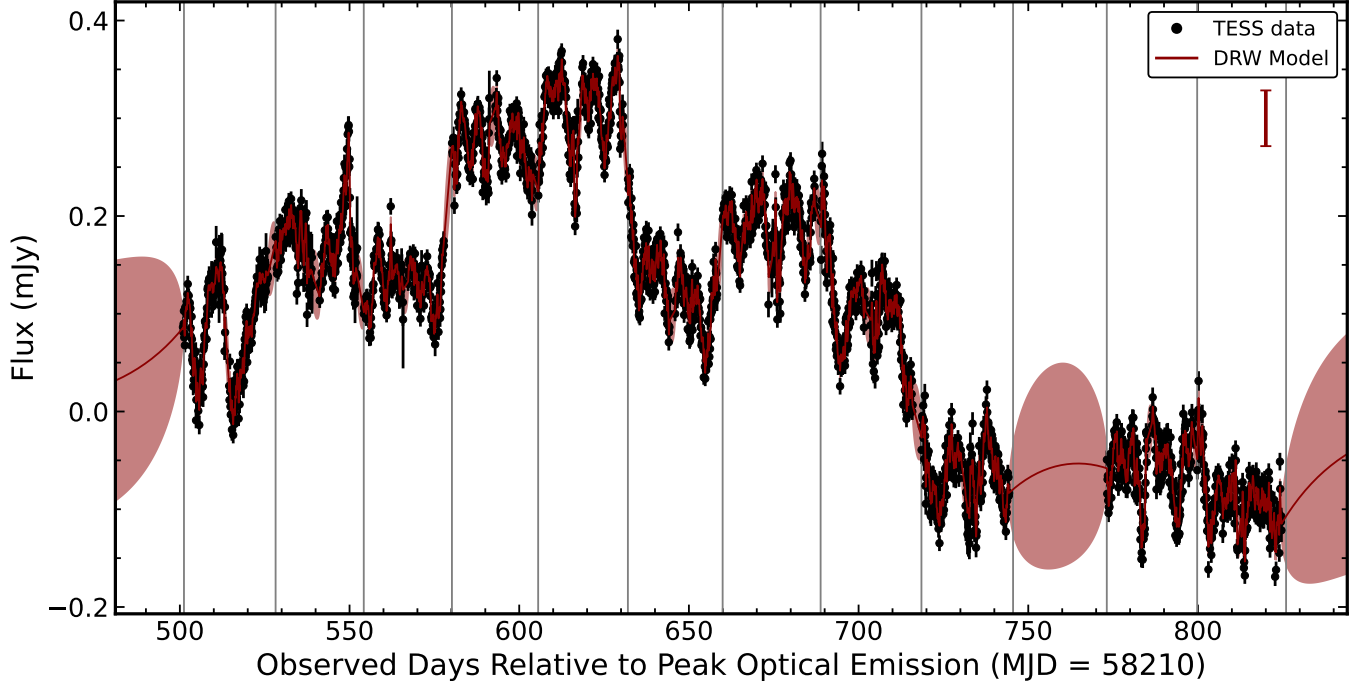
Figure 3. TESS data stacked in 2-hour bins (black points) with the mean DRW light curve shown in red. Here, no correction for Galactic extinction has been applied. The shading represents the RMS of the DRW light curves. The range of allowed light curves broadens rapidly when there is no data in a given time interval. The vertical gray bars mark the beginning of new sectors. In this model, linear offsets are computed between the sectors such that the global mean flux is zero. The inter-sector calibration has larger errors than the point-to-point precision in the TESS light curve (shown as the error bar in the upper right) but these uncertainties are included in our analysis and do not affect our results.
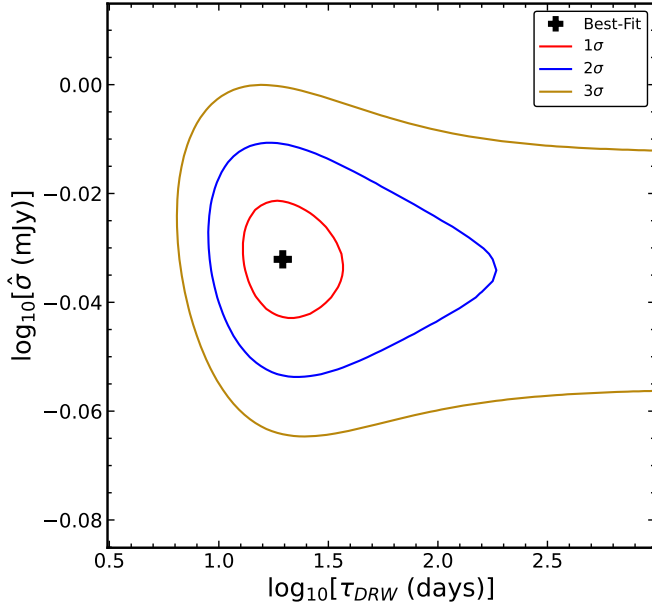
Figure 4. Contours of $\log(\hat{\sigma})$ and $\log(\tau_{DRW})$, shown at 1, 2, and 3σ from the best-fit value shown as a black cross. The values of $\hat{\sigma}$ and τ have been corrected into the rest frame using the host redshift of z = 0.01905 and $\hat{\sigma}$ has been corrected for Galactic extinction.

a smooth transition to a f^{-2} power-law (red noise) at higher frequencies. The parameters of the model are the characteristic timescale τ_{DRW} and the amplitude $\hat{\sigma} = \sigma(\frac{2 \times 365.25 \text{ d}}{\tau_{DRW}})^{1/2}$.

Following Kozłowski et al. (2010), we fit the observed TESS light curve from Sectors 15-26 allowing for an independent flux offset for each sector (these are simply additional linear parameters in the model). This provides a well-defined statistical means of including the non-adjacent data in Sectors 25-26, drives the mean flux to zero, and includes all the uncertainties from these flux offsets into the estimates of $\hat{\sigma}$ and τ_{DRW}. The magnitude of the median offset is 57 μJy with a dispersion of 83 μJy. We binned our TESS light curve in 2-hour bins so that the light curve has a reasonable signal-to-noise ratio per binned epoch. Throughout the remainder of this manuscript, we use these flux offsets to calibrate the fluxes for each individual Cycle 2 sector relative to the first TESS sector. However, we note that the inter-sector calibration likely has larger errors than the point-to-point precision in the TESS light curve, and long timescale trends should be viewed with caution.

The contours for variability timescale and amplitude are shown in Figure 4, with the parameters corrected for source redshift and Galactic extinction. At the 1σ level,
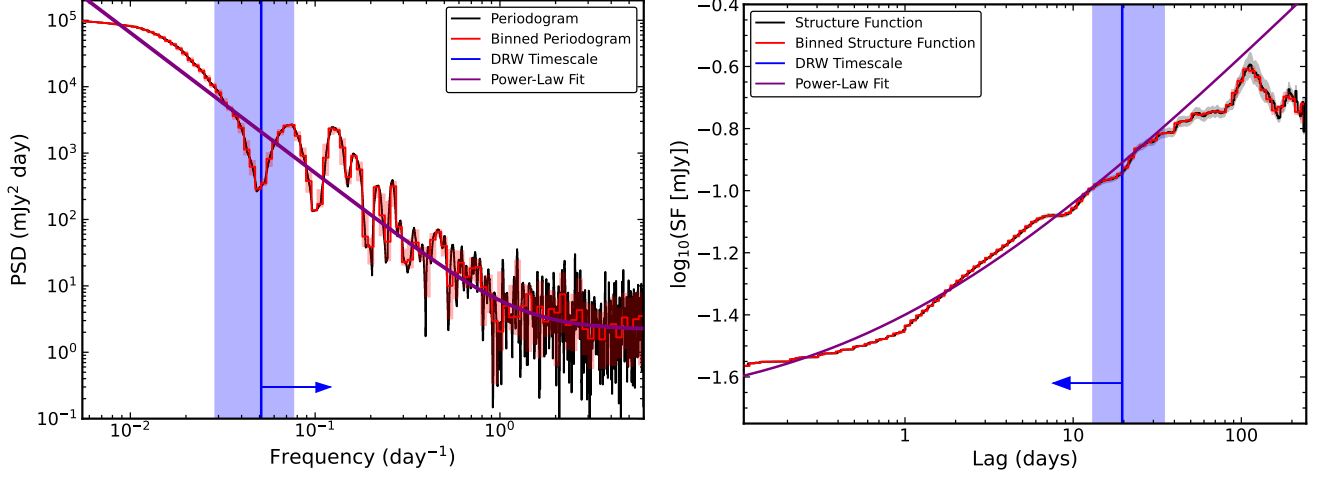
Figure 5. Power spectral density (left panel) and structure function (right panel) of the 2-hour binned TESS light curve. The PSD is computed using SCIPY.SIGNAL.PERIODOGRAM. The red lines represent the PSD and SF binned in 100 logarithmic bins and the red shading indicates the 1σ scatter over that bin width. The gray band around the SF is the uncertainty at that lag. The blue lines are the estimated τ_{DRW}, with the shading representing the uncertainty. As expected, the best-fit τ_{DRW} roughly coincides with the break in the PSD from a flat white noise to the higher frequency power-law slope. The purple lines are a power-law fits, with the PSD fit giving $\alpha = -2.11$ and the SF fit yielding $\gamma = 0.54$, both consistent with the expectations of a DRW model. The blue arrows represent the regions over which the power-law fits are done.

the contours are well-behaved, but the upper bound on τ_{DRW} increases rapidly at higher confidence. The characteristic timescale of $\tau_{DRW} = 20^{+15}_{-6}$ days is similar to those found for other AGNs with similar mass SMBHs (e.g., Kelly et al. 2009; Burke et al. 2021). The variability amplitude of $\hat{\sigma} = 0.93 \pm 0.02$ mJy, corresponding to $\sigma \sim 0.13$ mJy for the above τ_{DRW}, is large, immediately suggestive of AGN-like variability.

We tested how our decisions on connecting individual TESS sectors together affected our results, finding that regardless of how we match adjoining sectors, the recovered τ_{DRW} values are consistent within 1σ uncertainties. The variability amplitude σ is much more sensitive to choices on sector matching, but we are able to directly compute the RMS scatter for each TESS sector, circumventing the DRW modeling and sector-matching entirely. The median RMS scatter per sector is 24 μJy, which is 8% of the median TESS flux over the same range.

Figure 5 shows the PSD and structure function (SF) of the TESS light curve of ASASSN-18el between Sectors 15 and 23, avoiding the sector-long gaps in the TESS coverage. The PSD was computed using SCIPY.SIGNAL.PERIODOGRAM and a flat top window function to increase amplitude accuracy. As expected from previous studies of AGN variability (e.g., Mushotzky et al. 2011; Kozłowski 2017), the PSD is flat at low frequencies, with a declining power-law at higher frequencies. Similarly, the SF is roughly flat at long lags with a declining slope towards shorter lags. At the

highest frequencies (shortest lags), the PSD (SF) flattens again as the signal becomes dominated by photometric noise. There is also a dip in the PSD at ~ 0.04 day^{-1}, likely due to the 27 day length of the TESS sector and the linear offsets applied between the sectors. If we fit the PSD above the measured value of τ_{DRW} (in frequency) with a single power-law plus a photometric noise term, we find a power-law index of $\alpha = -2.11 \pm 0.16$. Likewise, if we fit the SF below the measured value of τ_{DRW} (in time) with the same model we find a power-law index of $\gamma = 0.54 \pm 0.02$.

The canonical power-law slope for a DRW model is $\alpha = -2$ (e.g., Zu et al. 2011, 2013) for the PSD and $\gamma = 0.5$ (e.g., Kozłowski 2016) for the SF. Studies of AGNs using high-quality Kepler light curves (Mushotzky et al. 2011; Smith et al. 2018) have shown a range of power-law slopes between $\alpha = -1.7$ and $\alpha = -3.3$, although Moreno et al. (2021) showed that Kepler systematics can mimic AGN variability. Therefore, we find that the power-law slopes for the PSD and SF of ASASSN-18el are fully consistent with other optical AGNs and with the theoretical assumptions made when fitting the TESS light curve with a DRW model.

3.3. *Optical/X-ray Correlation*

Next we searched for a correlation between the TESS optical and NICER X-ray light curves, shown in Figure 6. The X-ray emission is roughly an order of magnitude higher than the optical emission at the same phase, unlike many other ANTs (Neustadt et al. 2020; Hinkle et al. 2021c). Qualitatively, both light curves show a
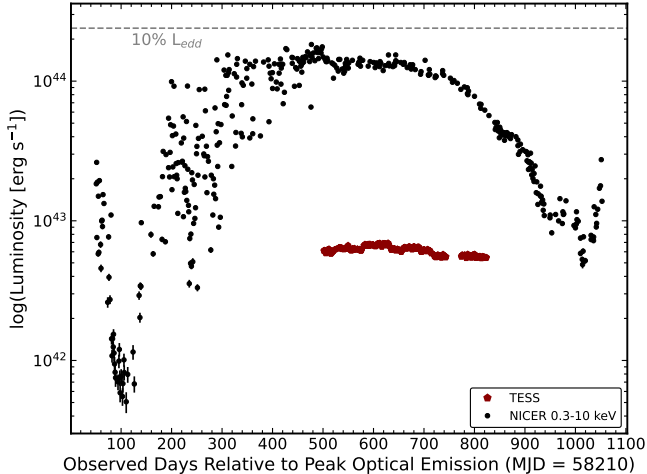
Figure 6. NICER (black circles) and TESS (dark red pentagons) light curves of ASASSN-18el. The NICER luminosity is integrated over the 0.3-10 keV bandpass and the TESS luminosity is λL_λ at the pivot wavelength of the TESS bandpass. It is clear that the X-ray component of the emission is more than an order of magnitude more luminous than the optical component during the time of overlapping data.

plateau over the time period from 500 to 700 days after the peak emission, where they overlap. After this plateau, both the NICER and TESS light curves begin to decline. This is likely due to a change in the overall accretion rate onto the central SMBH.

We tried to measure a temporal lag between the NICER and TESS light curves. If the optical variability was a result of the reprocessing of the far more luminous X-rays, we would expect to see a correlation between light curve features in the X-ray and the optical, with the optical lagging behind the X-ray. Assuming this is due to light travel time, this lag would give an approximate physical size of the accretion disk between the X-ray emitting corona and the cooler portions of the disk from which the emission seen in the TESS bandpass originate. Unfortunately, neither the straightforward cross-correlation function code PYCCF (Sun et al. 2018) nor the more sophisticated DRW modeling code JAVELIN (Zu et al. 2011, 2013) model produced a useful result. Additionally, we tested if binning the TESS data and/or smoothing the light curves to remove long-term trends affected the lag fits, but neither was able to return an acceptable result.

3.4. *Very Late-time Data*

After TESS returned to the Northern hemisphere in Cycle 4, ASASSN-18el was observed again. We show the full TESS light curve as of the end of 2021, including Sectors 15-23, 25-26, and 40-41 in Figure 7. It is immediately clear that the rapid high-amplitude variability

has faded by the very-late time sectors. To quantify the change in variability amplitude between the early and late sectors, we measured the RMS scatter in the first sector and compared it to the last sector. For Sector 15, the RMS scatter around the median flux is 46 μJy. Roughly 2 years later in Sector 41, the RMS scatter had dropped by a factor of almost 5 to 9 μJy. ASASSN-18el will be observed in 13 continuous TESS sectors in Cycles 4 and 5 (Sectors 47 - 59), allowing for additional late-time monitoring of the source variability well after the transient has faded.

While the overall light curve shape is not particularly important for understanding the short-term variability expected of AGNs, we used stacked late-time ATLAS data to measure the o-band flux concurrent with active TESS sectors to allow us to create a long-term TESS light curve. We matched the first TESS sector to the concurrent ATLAS o-band flux and applied the linear offsets between sectors computed in the DRW modeling to calibrate the flux of the remaining Cycle 2 TESS sectors. For the Cycle 4 TESS light curves, we added the concurrent ATLAS o-band flux to the differential TESS light curve. As our primary aim in Figure 7 is to show the consistent strong short-term variability of ASASSN-18el over a 2 year time span, details on sector to sector matching are largely inconsequential.

4. DISCUSSION

Two plausible explanations have been put forward to explain the changing-look phenomenon observed for the ANT ASASSN-18el. The first is related to instabilities in the existing AGN disk, either as a result of a change in the accretion flow (Trakhtenbrot et al. 2019b) or something more exotic like a magnetic inversion in the disk (Scepi et al. 2021; Laha et al. 2022). The second is increased accretion due to a TDE, which disrupted the existing X-ray corona while powering a large UV/optical flare (Ricci et al. 2020).

The variability seen in the TESS light curve is typical of known AGNs and consistent with the DRW model frequently used to describe AGN variability. Both the PSD and SF of the TESS light curve are typical of AGNs. Therefore, independent of any modeling of the TESS light curve and choices on sector matching, this short-term stochastic variability suggests an AGN origin for ASASSN-18el.

Nevertheless, with a measurement of τ_{DRW}, we can compare to known relationships, such as the one between τ_{DRW} and the central SMBH mass, shown in Figure 8. As the black hole mass increases, so does the characteristic timescale, resulting from the scaling of accretion disk parameters (e.g., Kelly et al. 2009; Zu et al. 2013).
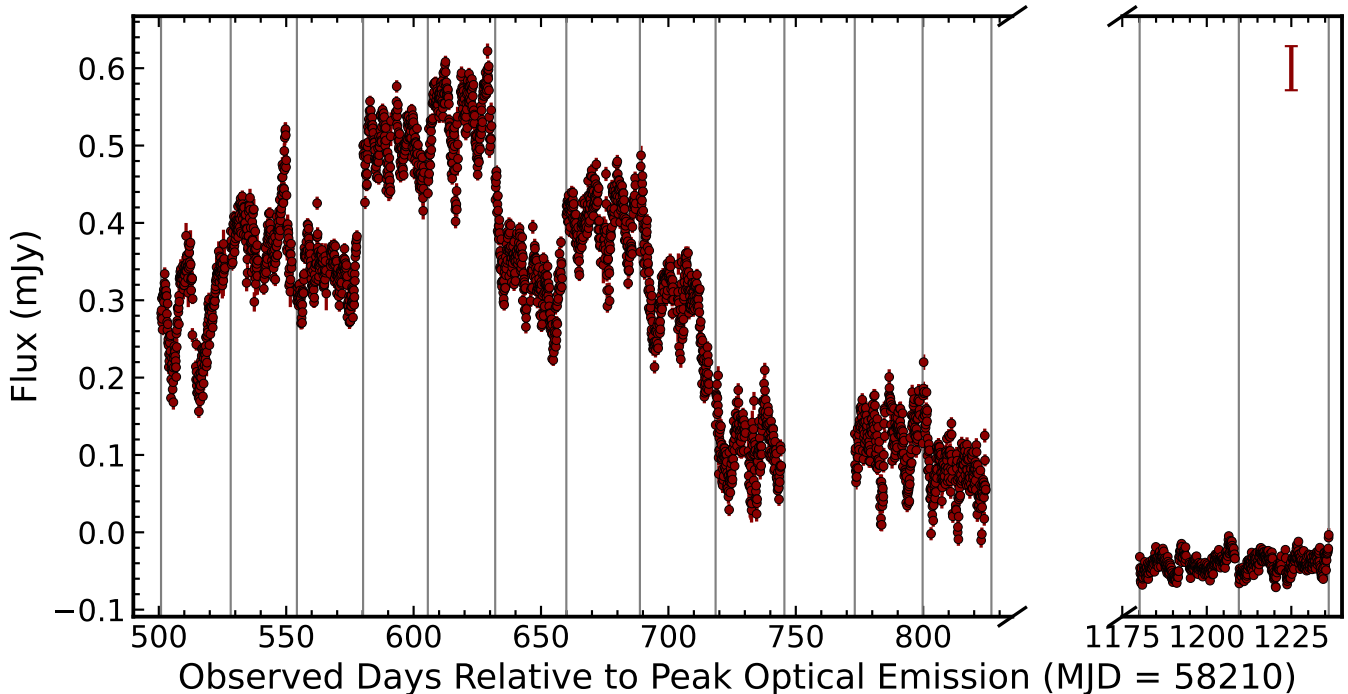
Figure 7. TESS data stacked in 2 hr bins (red points) spanning from the initial Sector 15 light curve to the very late-time Sector 41 light curve. The vertical gray bars mark the beginning of new sectors and the error bar in the upper right indicates the median magnitude of the sector-to-sector offsets.

In particular, Burke et al. (2021) suggest that the characteristic variability timescale is linked to the thermal timescale for the UV-emitting region of the accretion disk, even when that τ_{DRW} is measured with optical rather than UV photometry. ASASSN-18el lies near the trend between τ_{DRW} and SMBH mass. In Figure 8 we have shown both the original best-fit line and our fit to the data from Kelly et al. (2009) using the MCMC procedure of Kelly (2007) to better illustrate the range of allowed slopes for this relationship given many sources with large uncertainties.

Similarly, we can compare the pre-flare constraints from ASAS-SN and ATLAS on variability to those obtained with TESS. Prior to the flare, there are only hints of weak activity, with sparse detections in the ASAS-SN V-band photometry. This is consistent with the archival Seyfert 2 classification of the AGN 1ES 1927+654. The lack of strong variability prior to the flare in contrast with short-timescale variability seen during the flare suggests that ASASSN-18el is an example of an increase in the accretion rate onto the AGN rather than a TDE. This scenario is also consistent with the late-time decrease in variability, as the AGN begins to return to its quiescent state.

It is important to note that there are some caveats to the analysis of AGN light curves using a DRW model. The primary concern is the length of the light curve

relative to the recovered timescale. Recent simulations suggest that for robust recovery of DRW parameters, the length of the light curve should be at least ten times the τ_{DRW} (e.g., Kozłowski 2017, 2021), with shorter light curves biased towards shorter timescales. For ASASSN-18el the length of the TESS light curve is roughly 16 times longer than the recovered τ_{DRW}. Figure 4 of Kozłowski (2021) suggests that there is only a ~ 0.1 dex uncertainty in τ_{DRW} at this length. Even if the true τ_{DRW} for ASASSN-18el was underestimated by a few tenths of a dex, it would remain close to the trend shown in Fig. 8. Finally, as noted in Section 3.2, results related to the long-timescale trends in the TESS light curve should be viewed with caution because of uncertainties and systematic issues associated with the inter-sector calibrations.

Finally, with respect to the possibility that the changing-look phenomenon was caused by a TDE, it is difficult to explain the observed variability in the context of TDE emission. To date only a small number of TDEs have exhibited any stochastic variability (e.g., Holoien et al. 2019), and TDE light curves typically do not exhibit re-brightening episodes like the ones seen here in ATLAS and ASAS-SN photometry. Late-time studies of TDEs have suggested a shift in the emission mechanism from one tied to the fallback of mass onto the SMBH to emission from the accretion disk itself (Balbus & Mum-
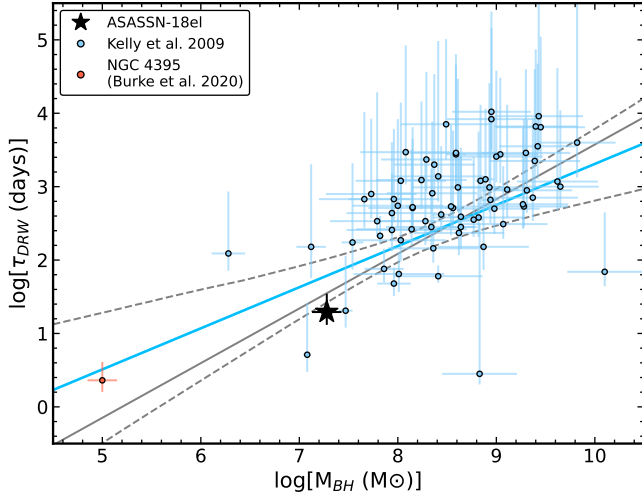
Figure 8. The rest-frame DRW timescale (τ_{DRW}) as compared to the SMBH mass for a given AGN. The sample of Kelly et al. (2009) is shown in light blue, with their best-fit line shown with the light blue solid line. The solid gray line is our fit of the Kelly et al. (2009) sample using the methods of Kelly (2007). The dashed gray lines are plus/minus one sigma from the best-fit line. Both NGC 4395 (Burke et al. 2020) and ASASSN-18el are excluded from this fit.

mery 2018; van Velzen et al. 2019; Jonker et al. 2020). A natural assumption is that, similar to AGN disks, this may lead to enhanced variability from instabilities in disk. Nonetheless, when examining late-time data on the TDEs ASASSN-14ae and ASASSN-14li (van Velzen et al. 2019; Hinkle et al. 2021a), we find that there is no significant variability on several day timescales even long after disk emission is thought to become the dominant component for these sources (van Velzen et al. 2019). This suggests that a TDE transitioning to a disk-dominated state is unlikely to show the very large variability that we see from ASASSN-18el at similarly late times. In addition, the long overall timescale of the event is not consistent with known TDEs (e.g., Holoien et al. 2014b, 2016a,b; Hinkle et al. 2020). These suggest that a TDE is likely not the source of the transient emission for ASASSN-18el.

5. SUMMARY

Through our analysis of late-time optical photometry, NICER X-ray data, and a high-cadence TESS light curve of ASASSN-18el we find the following:

- Optical transient emission from ASASSN-18el remains detectable above pre-flare levels for roughly 700 days after the peak optical emission with late-time re-brightening episodes continuing until at least 1250 days after peak.

- The initial decline of ASASSN-18el as measured from the ATLAS o-band light curve is significantly flatter than the canonical $t^{-5/3}$ power-law for TDEs. Additionally, when the decline is fit by an exponential-decay model, the timescale of the decline is roughly three times longer than observed for typical TDEs.

- The high-S/N and high-cadence TESS light curve within 1000 days of peak optical emission shows strong variability on timescales less than a single TESS sector, immediately suggestive of strong AGN activity.

- The TESS light curve's large variability amplitude and characteristic timescale are consistent with light curves of AGNs with similar SMBH masses, supporting the claim that the observed transient emission at late times is fully consistent with a dramatic AGN flare. However, there are large uncertainties and potential systematic errors related to the long-timescale trends in the TESS light curve.

- The X-ray and optical evolution is distinct, with large dips in X-ray luminosity at early and late times despite a relatively smooth optical light curve. However, during the period of overlap between TESS and NICER data, a multi-wavelength plateau phase is observed. Nonetheless, we were unable to recover a temporal lag between the X-ray and TESS bandpasses.

- The very late-time TESS data (more than 1000 days after peak emission) continues to show stochastic variability, but at a lower amplitude than earlier sectors.

From our analysis of these late-time data, and in particular the exquisite TESS data, we find that the flare in ASASSN-18el is likely the result of a large AGN flare. Many of the optical changing-look AGNs to date lack the wealth of data presented here. However, the few that do, such as NGC 2617 (Shappee et al. 2014) and ASASSN-18el may suggest that such state changes are not always long term but rather may be the result of large flares.

The use of TESS and its unparalleled combination of photometric precision, cadence, and sky coverage is a promising avenue for studying the physical origin of ANTs. TESS observations of an ANT at any phase can give detailed insight into the variability properties of a galaxy. At the very least, a sector of TESS data should be able to uncover the presence of AGN-like variability in ANT host galaxies, well below what can be probed

from the ground. This gives promise that we can begin to understand the range of nuclear behaviors and accretion processes through the disambiguation of ANTs.

REFERENCES

Alard, C. 2000, A&AS, 144, 363, doi: 10.1051/aas:2000214

Alard, C., & Lupton, R. H. 1998, ApJ, 503, 325, doi: 10.1086/305984

Auchettl, K., Guillochon, J., & Ramirez-Ruiz, E. 2017, ApJ, 838, 149, doi: 10.3847/1538-4357/aa633b

Balbus, S. A., & Mummery, A. 2018, MNRAS, 481, 3348, doi: 10.1093/mnras/sty2467

Barron, J. T., Stumm, C., Hogg, D. W., Lang, D., & Roweis, S. 2008, AJ, 135, 414, doi: 10.1088/0004-6256/135/1/414

Bennett, C. L., Larson, D., Weiland, J. L., & Hinshaw, G. 2014, ApJ, 794, 135, doi: 10.1088/0004-637X/794/2/135

Bianchi, S., Guainazzi, M., Matt, G., et al. 2005, A&A, 442, 185, doi: 10.1051/0004-6361:20053389

Bogdanov, S., Guillot, S., Ray, P. S., et al. 2019, ApJL, 887, L25, doi: 10.3847/2041-8213/ab53eb

Boller, T., Voges, W., Dennefeld, M., et al. 2003, A&A, 397, 557, doi: 10.1051/0004-6361:20021520

Brown, T. M., Baliber, N., Bianco, F. B., et al. 2013, PASP, 125, 1031, doi: 10.1086/673168

Burke, C. J., Shen, Y., Chen, Y.-C., et al. 2020, ApJ, 899, 136, doi: 10.3847/1538-4357/aba3ce

Burke, C. J., Shen, Y., Blaes, O., et al. 2021, Science, 373, 789, doi: 10.1126/science.abg9933

Denney, K. D., De Rosa, G., Croxall, K., et al. 2014, ApJ, 796, 134, doi: 10.1088/0004-637X/796/2/134

Drake, A. J., Djorgovski, S. G., Mahabal, A., et al. 2009, ApJ, 696, 870, doi: 10.1088/0004-637X/696/1/870

Evans, C. R., & Kochanek, C. S. 1989, ApJL, 346, L13, doi: 10.1086/185567

Frederick, S., Gezari, S., Graham, M. J., et al. 2019, ApJ, 883, 31, doi: 10.3847/1538-4357/ab3a38

—. 2021, ApJ, 920, 56, doi: 10.3847/1538-4357/ac110f

Gendreau, K. C., Arzoumanian, Z., & Okajima, T. 2012, Society of Photo-Optical Instrumentation Engineers (SPIE) Conference Series, Vol. 8443, The Neutron star Interior Composition ExploreR (NICER): an Explorer mission of opportunity for soft x-ray timing spectroscopy, 844313, doi: 10.1117/12.926396

Gezari, S., Chornock, R., Rest, A., et al. 2012, Nature, 485, 217, doi: 10.1038/nature10990

Giacconi, R., Branduardi, G., Briel, U., et al. 1979, ApJ, 230, 540, doi: 10.1086/157110

Guo, H., Peng, J., Zhang, K., et al. 2020, ApJ, 905, 52, doi: 10.3847/1538-4357/abc2ce

Haggard, D., Green, P. J., Anderson, S. F., et al. 2010, ApJ, 723, 1447, doi: 10.1088/0004-637X/723/2/1447

Henden, A. A., Levine, S., Terrell, D., & Welch, D. L. 2015, in American Astronomical Society Meeting Abstracts, Vol. 225, American Astronomical Society Meeting Abstracts #225, 336.16

Hinkle, J. T., Holoien, T. W. S., Shappee, B. J., & Auchettl, K. 2021a, ApJ, 910, 83, doi: 10.3847/1538-4357/abe4d8

Hinkle, J. T., Holoien, T. W. S., Shappee, B. J., et al. 2020, arXiv e-prints, arXiv:2001.08215. https://arxiv.org/abs/2001.08215

Hinkle, J. T., Holoien, T. W. S., Auchettl, K., et al. 2021b, MNRAS, 500, 1673, doi: 10.1093/mnras/staa3170

Hinkle, J. T., Holoien, T. W. S., Shappee, B. J., et al. 2021c, arXiv e-prints, arXiv:2108.03245. https://arxiv.org/abs/2108.03245

Ho, L. C. 2008, ARA&A, 46, 475, doi: 10.1146/annurev.astro.45.051806.110546

Holoien, T. W.-S., Prieto, J. L., Stanek, K. Z., et al. 2014a, ApJL, 785, L35, doi: 10.1088/2041-8205/785/2/L35

Holoien, T. W.-S., Prieto, J. L., Bersier, D., et al. 2014b, MNRAS, 445, 3263, doi: 10.1093/mnras/stu1922

Holoien, T. W.-S., Kochanek, C. S., Prieto, J. L., et al. 2016a, MNRAS, 455, 2918, doi: 10.1093/mnras/stv2486

—. 2016b, MNRAS, 463, 3813, doi: 10.1093/mnras/stw2272

Holoien, T. W.-S., Brown, J. S., Vallely, P. J., et al. 2019, MNRAS, 484, 1899, doi: 10.1093/mnras/stz073

Holoien, T. W. S., Auchettl, K., Tucker, M. A., et al. 2020, arXiv e-prints, arXiv:2003.13693. https://arxiv.org/abs/2003.13693

Holoien, T. W. S., Neustadt, J. M. M., Vallely, P. J., et al. 2021, arXiv e-prints, arXiv:2109.07480. https://arxiv.org/abs/2109.07480

Jonker, P. G., Stone, N. C., Generozov, A., van Velzen, S., & Metzger, B. 2020, ApJ, 889, 166, doi: 10.3847/1538-4357/ab659c

Kelly, B. C. 2007, ApJ, 665, 1489, doi: 10.1086/519947

Kelly, B. C., Bechtold, J., & Siemiginowska, A. 2009, ApJ, 698, 895, doi: 10.1088/0004-637X/698/1/895

Kochanek, C. S., Shappee, B. J., Stanek, K. Z., et al. 2017, PASP, 129, 104502, doi: 10.1088/1538-3873/aa80d9

Kozłowski, S. 2016, ApJ, 826, 118, doi: 10.3847/0004-637X/826/2/118

—. 2017, A&A, 597, A128, doi: 10.1051/0004-6361/201629890

—. 2021, arXiv e-prints, arXiv:2109.03896. https://arxiv.org/abs/2109.03896

Kozłowski, S., Kochanek, C. S., Udalski, A., et al. 2010, ApJ, 708, 927, doi: 10.1088/0004-637X/708/2/927

Lacerda, E. A. D., Sánchez, S. F., Cid Fernandes, R., et al. 2020, MNRAS, 492, 3073, doi: 10.1093/mnras/staa008

Laha, S., Meyer, E., Roychowdhury, A., et al. 2022, arXiv e-prints, arXiv:2203.07446. https://arxiv.org/abs/2203.07446

LaMassa, S. M., Cales, S., Moran, E. C., et al. 2015, ApJ, 800, 144, doi: 10.1088/0004-637X/800/2/144

Lang, D., Hogg, D. W., Mierle, K., Blanton, M., & Roweis, S. 2010, AJ, 139, 1782, doi: 10.1088/0004-6256/139/5/1782

Leloudas, G., Dai, L., Arcavi, I., et al. 2019, arXiv e-prints. https://arxiv.org/abs/1903.03120

Lupton, R. 2005, http://www.sdss.org/dr5/algorithms/sdssUBVRITransform.html

MacLeod, C. L., Ivezić, Ž., Kochanek, C. S., et al. 2010, ApJ, 721, 1014, doi: 10.1088/0004-637X/721/2/1014

MacLeod, C. L., Ivezić, Ž., Sesar, B., et al. 2012, ApJ, 753, 106, doi: 10.1088/0004-637X/753/2/106

Malyali, A., Rau, A., Merloni, A., et al. 2021, A&A, 647, A9, doi: 10.1051/0004-6361/202039681

Moreno, J., Buttry, R., O'Brien, J., et al. 2021, AJ, 162, 232, doi: 10.3847/1538-3881/ac205c

Mushotzky, R. F., Edelson, R., Baumgartner, W., & Gandhi, P. 2011, ApJL, 743, L12, doi: 10.1088/2041-8205/743/1/L12

Neustadt, J. M. M., Holoien, T. W. S., Kochanek, C. S., et al. 2020, MNRAS, 494, 2538, doi: 10.1093/mnras/staa859

Nicholls, B., Brimacombe, J., Kiyota, S., et al. 2018, The Astronomer's Telegram, 11391, 1

Payne, A. V., Shappee, B. J., Hinkle, J. T., et al. 2021, ApJ, 910, 125, doi: 10.3847/1538-4357/abe38d

Phinney, E. S. 1989, Nature, 340, 595, doi: 10.1038/340595a0

Rees, M. J. 1988, Nature, 333, 523, doi: 10.1038/333523a0

Ricci, C., Trakhtenbrot, B., Koss, M. J., et al. 2017, ApJS, 233, 17, doi: 10.3847/1538-4365/aa96ad

Ricci, C., Kara, E., Loewenstein, M., et al. 2020, ApJL, 898, L1, doi: 10.3847/2041-8213/ab91a1

Ricci, C., Loewenstein, M., Kara, E., et al. 2021, ApJS, 255, 7, doi: 10.3847/1538-4365/abe94b

Ricker, G. R., Winn, J. N., Vanderspek, R., et al. 2015, Journal of Astronomical Telescopes, Instruments, and Systems, 1, 014003, doi: 10.1117/1.JATIS.1.1.014003

Scepi, N., Begelman, M. C., & Dexter, J. 2021, MNRAS, 502, L50, doi: 10.1093/mnrasl/slab002

Schlafly, E. F., & Finkbeiner, D. P. 2011, ApJ, 737, 103, doi: 10.1088/0004-637X/737/2/103

Shappee, B. J., Prieto, J. L., Grupe, D., et al. 2014, ApJ, 788, 48, doi: 10.1088/0004-637X/788/1/48

Smith, K. L., Mushotzky, R. F., Boyd, P. T., et al. 2018, ApJ, 857, 141, doi: 10.3847/1538-4357/aab88d

Smith, K. W., Smartt, S. J., Young, D. R., et al. 2020, arXiv e-prints, arXiv:2003.09052. https://arxiv.org/abs/2003.09052

Sun, M., Grier, C. J., & Peterson, B. M. 2018, PyCCF: Python Cross Correlation Function for reverberation mapping studies. http://ascl.net/1805.032

Tonry, J. L., Denneau, L., Heinze, A. N., et al. 2018a, PASP, 130, 064505, doi: 10.1088/1538-3873/aabadf

Tonry, J. L., Denneau, L., Flewelling, H., et al. 2018b, ApJ, 867, 105, doi: 10.3847/1538-4357/aae386

Trakhtenbrot, B., Arcavi, I., Ricci, C., et al. 2019a, Nature Astronomy, 3, 242, doi: 10.1038/s41550-018-0661-3

Trakhtenbrot, B., Arcavi, I., MacLeod, C. L., et al. 2019b, ApJ, 883, 94, doi: 10.3847/1538-4357/ab39e4

Tran, H. D., Lyke, J. E., & Mader, J. A. 2011, ApJL, 726, L21, doi: 10.1088/2041-8205/726/2/L21

Ulrich, M.-H., Maraschi, L., & Urry, C. M. 1997, ARA&A, 35, 445, doi: 10.1146/annurev.astro.35.1.445

Vallely, P. J., Kochanek, C. S., Stanek, K. Z., Fausnaugh, M., & Shappee, B. J. 2021, MNRAS, 500, 5639, doi: 10.1093/mnras/staa3675

Vallely, P. J., Fausnaugh, M., Jha, S. W., et al. 2019, MNRAS, 487, 2372, doi: 10.1093/mnras/stz1445

van Velzen, S., Stone, N. C., Metzger, B. D., et al. 2019, ApJ, 878, 82, doi: 10.3847/1538-4357/ab1844

van Velzen, S., Farrar, G. R., Gezari, S., et al. 2011, ApJ, 741, 73, doi: 10.1088/0004-637X/741/2/73

van Velzen, S., Gezari, S., Hammerstein, E., et al. 2021, ApJ, 908, 4, doi: 10.3847/1538-4357/abc258

Vanderspek, R., Doty, J., Fausnaugh, M., et al. 2018, TESS Instrument Handbook, Tech. rep., Kavli Institute for Astrophysics and Space Science, Massachusetts Institute of Technology

Vaughan, S., Edelson, R., Warwick, R. S., & Uttley, P. 2003, MNRAS, 345, 1271, doi: 10.1046/j.1365-2966.2003.07042.x

Villanueva, Steven, J., Gaudi, B. S., Pogge, R. W., et al. 2018, PASP, 130, 015001, doi: 10.1088/1538-3873/aa9603

Villanueva, S., Eastman, J. D., Gaudi, B. S., et al. 2016, in Society of Photo-Optical Instrumentation Engineers (SPIE) Conference Series, Vol. 9906, Ground-based and Airborne Telescopes VI, ed. H. J. Hall, R. Gilmozzi, & H. K. Marshall, 99062L, doi: 10.1117/12.2231122

Wright, E. L. 2006, PASP, 118, 1711, doi: 10.1086/510102

Wyrzykowski, Ł., Zieliński, M., Kostrzewa-Rutkowska, Z., et al. 2017, MNRAS, 465, L114, doi: 10.1093/mnrasl/slw213

Zu, Y., Kochanek, C. S., Kozłowski, S., & Udalski, A. 2013, ApJ, 765, 106, doi: 10.1088/0004-637X/765/2/106

Zu, Y., Kochanek, C. S., & Peterson, B. M. 2011, ApJ, 735, 80, doi: 10.1088/0004-637X/735/2/80